In vivo NIR-II structured-illumination light-sheet microscopy

Feifei Wang[a,b,1], Zhuoran Ma[a,b,1], Yeteng Zhong[a,b], Felix Salazar[c], Chun Xu[a,b], Fuqiang Ren[a,b], Liangqiong Qu[d], Anna M. Wu[c], and Hongjie Dai[a,b,2]

[a]Department of Chemistry, Stanford University, Stanford, CA 94305; [b]Bio-X, Stanford University, Stanford, CA 94305; [c]Molecular Imaging and Therapy, Beckman Research Institute, City of Hope, Duarte, CA 91010; and [d]School of Medicine, Stanford University, Stanford, CA 94303

Contributed by Hongjie Dai, December 17, 2020 (sent for review November 19, 2020; reviewed by Weibo Cai and Ke Xu)

Noninvasive optical imaging with deep tissue penetration depth and high spatiotemporal resolution is important to longitudinally studying the biology at the single-cell level in live mammals, but has been challenging due to light scattering. Here, we developed near-infrared II (NIR-II) (1,000 to 1,700 nm) structured-illumination light-sheet microscopy (NIR-II SIM) with ultralong excitation and emission wavelengths up to $\sim$1,540 and $\sim$1,700 nm, respectively, suppressing light scattering to afford large volumetric three-dimensional (3D) imaging of tissues with deep-axial penetration depths. Integrating structured illumination into NIR-II light-sheet microscopy further diminished background and improved spatial resolution by approximately twofold. In vivo oblique NIR-II SIM was performed noninvasively for 3D volumetric multiplexed molecular imaging of the CT26 tumor microenvironment in mice, longitudinally mapping out CD4, CD8, and OX40 at the single-cell level in response to immunotherapy by cytosine-phosphate-guanine (CpG), a Toll-like receptor 9 (TLR-9) agonist combined with OX40 antibody treatment. NIR-II SIM affords an additional tool for noninvasive volumetric molecular imaging of immune cells in live mammals.

light-sheet microscope | structured-illumination microscopy | near-infrared II imaging | noninvasive imaging

In vivo imaging and monitoring of cells through large volumes of tissues by high-resolution optical microscopy can afford details of complex biological structures and processes in live mammals, facilitating understanding of disease onset, progression, and response to therapy at the single-cell level (1, 2). Using planar illumination and orthogonal wide-field detection, light-sheet microscopy (LSM) is a powerful tool capable of fast three-dimensional (3D) imaging with low phototoxicity (3). Tremendous progress in several generations of LSM in the visible-light region has led to wide applications of fluorescence-based 3D biological imaging (2–15), for chemically cleared mammalian tissues with impressively large field of view (FOV) (10) and superresolution (11). High spatiotemporal 3D longitudinal imaging and tracking of small living organisms have also been realized (2, 16). Nevertheless, the penetration depth and resolution of visible-light LSM for imaging mammal tissues are limited by light scattering that causes light-sheet thickening/spreading as it propagates deeper into tissue, leading to reduction in axial resolution and FOV. Scattering of emitted fluorescence light depletes ballistic photons from deeper imaging planes, which also deteriorates signal-to-background ratio (SBR) and lateral resolution (17). Additionally, indigenous tissue autofluorescence in the visible region could further worsen the image contrast.

For mammalian imaging in vivo, currently visible-light LSM of mouse brain using one-photon excitation is limited to $\sim$200 μm depth after craniotomy to remove skull and scalp skin (10, 15). Two-photon (1,040 nm) light-sheet microscopy utilizing nonlinear excitation achieved deeper penetration up to $\sim$300 μm (for in vivo mouse brain imaging postcraniotomy) with high resolution owing to reduced scattering of the excitation light (6, 18). The penetration depth can be further increased using Bessel (19, 20) or Airy beams (21). Structured illumination has been used to modulate the excitation of Gaussian beam (22), Bessel beam (23–25), or lattice pattern (2, 14), providing a different approach to remove scattered fluorescence light, reject out-of-focus background, and enable thinner optical sectioning. Superresolution can be realized using structured illumination microscopy (SIM) (2, 12–14) by extracting high-frequency details embedded in low-resolution moiré fringes imaged under an illumination pattern at several shifted phases (26).

Recently we developed near-infrared II (NIR-II) LSM employing one-photon excitation and fluorescence emission detection in the near-infrared II window (1,000 to 1,700 nm) using fluorescent or luminescent organic dyes, quantum dots, and rare-earth down-conversion nanoparticles (17, 27–42). The suppressed light scattering and reduced tissue autofluorescence allowed noninvasive in vivo NIR-II LSM imaging through the scalp and skull of intact mouse head without craniotomy and through skin imaging of tumors without installing invasive optical windows, with a penetration depth up to $\sim$750 μm (17). Nevertheless, since the wavelength in the NIR-II window was approximately two to three times longer than visible light, the spatial resolution of NIR-II LSM was lower than that of visible LSM. Also, NIR-II imaging at deep tissues still experienced light scattering, causing background increase/decrease in the SBR and reduced spatial resolution.

Here, we developed oblique mode NIR-II SIM by integrating structured illumination into NIR-II LSM using the approach of digitally scanned laser beams (12, 13). We also employed PbS/CdS

Significance

Three-dimensional microscopy in the NIR-II window (1,000 to 1,700 nm) allows noninvasive deep-tissue optical sectioning of live mammals with high spatiotemporal resolution due to suppressed light scattering and reduced tissue autofluorescence. Herein, we present a NIR-II structured-illumination light-sheet microscopy (NIR-II SIM) with both excitation and emission wavelengths in the NIR-IIb window (1,500 to 1,700 nm). Integrating structured illumination into NIR-II light-sheet microscopy further diminished out-of-focus background and improved spatial resolution, facilitating in vivo imaging of cell behavior in the intact tissues without any invasive surgery during a long period. NIR-II SIM enabled longitudinally multiplexed molecular imaging of immune cells in response to immunotherapy in the tumor microenvironment.

Author contributions: F.W. and H.D. designed research; F.W. and Z.M. performed research; F.W., Z.M., Y.Z., F.S., C.X., F.R., L.Q., and A.M.W. contributed new reagents/analytic tools; F.W. and H.D. analyzed data; and F.W. and H.D. wrote the paper.

Reviewers: W.C., University of Wisconsin–Madison; and K.X., University of California, Berkeley.

The authors declare no competing interest.

[1]F.W. and Z.M. contributed equally to this work.

[2]To whom correspondence may be addressed. Email: hdai1@stanford.edu.

This article contains supporting information online at https://www.pnas.org/lookup/suppl/doi:10.1073/pnas.2023888118/-/DCSupplemental.

Published February 1, 2021.

core/shell quantum dot (CSQD) probes (28) to extend excitation and emission up to 1,540 nm and 1,600 to 1,700 nm, respectively. The benefits of suppressed scattering at longer wavelength, diminished out-of-focus background, and improved lateral resolution by structured illumination significantly enhanced the imaging capability of NIR-II SIM for both ex vivo and in vivo volumetric imaging.

Results

Suppressing Light-Scattering Background and Enhancing Resolution by NIR-II SIM. We developed a NIR-II LSM imaging technique with structured illumination in an oblique configuration (Fig. 1*A*), using a scanned Gaussian beam (20, 22) (Fig. 1 *A* and *B* and *SI Appendix*, Fig. S1). In each optical sectioning plane, the Gaussian beam was scanned in discrete steps to generate a comb-like excitation pattern and the pattern was generated in $k = 5$ phases (Fig. 1*B*). Each phase was created by laterally translating the comb pattern by n/k of one period ($n = 0, 1, \ldots, k - 1$). The k images recorded at all phases were then used to reconstruct a single image for the section (12). For in vivo imaging, the exposure time of the single-phase image was ∼100 to 150 ms. The 3D imaging was performed by repeating this process at successive planes.

We first calibrated NIR-II SIM resolution using 300-nm polystyrene beads containing an NIR-II organic dye (29) at different combinations of illumination and detection objectives. A 658-nm laser was used for excitation and the fluorescence emission was filtered by a 1,100-nm long-pass filter. For a typical experiment when 10× illumination (numerical aperture [NA] = 0.25) and 20× (NA = 0.4) detection objectives were used, the full width at half maximum (FWHM) of the 658-nm Gaussian excitation waist was ∼1.9 μm (double Rayleigh range was ∼35 μm). The period of structured illumination was 2.6 to 3.6 times the FWHM of the Gaussian excitation beam. For imaging the 300-nm beads, we found that the resolution in the y (beam-scan) direction of SIM was improved by ∼1.7 times compared to traditional LSM (Fig. 1 *C* and *D* and *SI Appendix*, Fig. S2), with $1.7 \times 1.1 \times 1.6$-μm and $2.0 \times 1.9 \times 2.0$-μm volumetric FWHMs with and without structured illumination, respectively. The measured LSM resolution was closed to diffraction-limited resolution of $1.9 \times 1.9 \times 1.9$ μm (*SI Appendix*, Fig. S2 and *Materials and Methods*) (17). The SBR was vastly improved from 11 to 171 when the structured illumination was used (Fig. 1*D*). The objectives combination determined the balance/compromise between spatial resolution and FOV.

Next, we performed experiments to compare NIR-II LSM with and without SIM at different excitation wavelengths. PbS/CdS CSQD probes (excitation and emission in the ranges of ultraviolet radiation to 1,550 nm and 1,500 to 1,700 nm, respectively; *SI Appendix*, Fig. S3) were intravenously injected into a mouse through the tail vein. The mouse was killed 10 min after injection when the probes were still in circulation, and the brain was fixed and preserved in glycerol for ex vivo imaging of brain vasculatures. As the excitation wavelength increased from 808 nm, to 1,319 nm (emission collected in 1,500 to 1,700 nm), to 1,540 nm (emission collected in 1,600 to 1,700 nm), increases in signal-to-noise ratio (SNR) of mouse cerebrovascular were clearly observed by NIR-II LSM (using traditional light sheet formed by a cylindrical lens) (17) (*SI Appendix*, Fig. S4), similar to the trend observed previously (17).

NIR-II SIM (by using a digitally scanned laser beam) further eliminated background and enhanced SNR and contrast (Fig. 1 *E*–*G* and *SI Appendix*, Fig. S4). With 808-nm excitation and 1,500- to 1,700-nm detection, SIM was unable to resolve vasculatures at penetration depths > ∼800 μm (*SI Appendix*, Fig. S4*A*) caused by light scattering deteriorating the structured-illumination pattern sharpness of the 808-nm excitation. In contrast, when 1,319- and 1,540-nm structured illuminations were used as excitation, the resulting 1,500- to 1,700-nm (1,319-nm excitation) and 1,600- to 1,700-nm (1,540-nm excitation) NIR-II SIM imaging was greatly improved (*SI Appendix*, Fig. S4). NIR-II SIM with both excitation and emission wavelengths >1,500 nm minimized scattering and increased SNR and imaging resolution (Fig. 1 *E*–*G* and *SI Appendix*, Fig. S5). It allowed large-FOV 3D NIR-II SIM imaging of glycerol-cleared mouse brain down to the hippocampus region, ∼1-mm deep underneath the surface of the cerebral cortex (Fig. 1 *F* and *G*). The background reduced and the SNR increased from 2.3, 4.4, and 37.0 to 5.4, 50.0, and 74.3 for 808-, 1,319-, and 1,540-nm excitations, respectively (Fig. 1*G*). Without SIM, the measured FWHMs of a vasculature (marked in Fig. 1*F*, at a depth of ∼1 mm in brain) imaged by NIR-LSM at 808-, 1,319-, and 1,540-nm excitations were 25, 19, and 19 μm, respectively. With SIM, the corresponding FWHMs decreased to 14, 13, and 9 μm, respectively, confirming improved spatial resolution by structured illumination by approximately a factor of 2 (12, 43).

Noninvasive In Vivo NIR-II SIM of Tumor Microenvironment Post-Cytosine-Phosphate-Guanine Treatment. Investigating the cellular signaling networks between cancer cells and their microenvironment in a tumor is important to devising effective anticancer strategies (44). Currently high-resolution molecular imaging of the tumor microenvironment mainly relies on invasive surgery or installing transparent optical windows (45) that requires complex procedures, long habituation period (46), and undesired stress and perturbation to mice, potentially leading to incorrect analysis of the immune response in immunotherapy. For example, it has been shown that mechanical disruption during surgery could trigger microglia and astrocyte activation (47, 48). The oblique configuration of NIR-II SIM affords noninvasive in vivo imaging of tumors in live mice, allowing long-term longitudinal imaging down to the cellular scale (Fig. 2*A*).

The unmethylated CG-enriched oligodeoxynucleotide (cytosine-phosphate-guanine [CpG]) is a toll-like receptor 9 (TLR9) ligand that can induce a systemic immune response for tumor treatment and elicit sustained tumor-specific long-term immune memory (49–51). OX40 is a costimulatory molecule expressed on both activated effector and regulatory T cells. Its signaling can promote effector T cell activation and inhibit regulatory T cells (52) to facilitate tumor cell killing (53–56). Their underlying immune responses have been intensively studied by ex vivo flow cytometry (50, 52, 54, 55, 57–59), immunohistochemistry (50, 60), or immunofluorescence staining (50, 57, 60) after euthanizing mice at various timepoints and by in vivo positron emission tomography (PET) (52) or fluorescence imaging (46, 57) on the whole-body length scale. The NIR-II SIM offers a tool for in vivo molecular imaging of the immune cells noninvasively with high resolution and longitudinal tracking and monitoring capabilities, facilitating the investigation of cellular immune responses in the tumor microenvironment in real space and real time.

We first performed 3D in vivo molecular imaging of CD8$^+$ T cells and OX40$^+$ cells inside a subcutaneous CT26 tumor (murine colon carcinoma) on a BALB/c mouse (Fig. 2). CpG (50 μg) was applied by intratumoral injection into one of the two CT26 tumors inoculated on the two hindlimbs. Twenty-four hours later, erbium-based rare-earth down-conversion nanoparticles (ErNPs) (30, 31) (excitation, 975 nm; emission, 1,500 to 1,700 nm) conjugated to anti-CD8 cys-diabody (61) (aCD8-ErNPs) and PEGylated PbS/CdS CSQD (excitation, 1,540 nm; emission, 1,600 to 1,700 nm) conjugated to anti-OX40 (aOX40-PbS) were injected intravenously through the tail vein. The blood circulation half times of PbS and ErNPs were ∼4.8 and ∼5.2 h, respectively (31, 42), over which these nanoprobes extravasated in the tumor as clearly imaged by in vivo LSM imaging in a noninvasive manner (*SI Appendix*, Fig. S6). On day 4, another dose of CpG was injected intratumorally (Fig. 2*B*). In another 24 h, we performed oblique NIR-II LSM and SIM to profile the 3D spatial distribution of aCD8-ErNPs and aOX40-PbS in the CT26 tumor microenvironment. The photoluminescences of ErNPs and PbS/CdS CSQD were in the

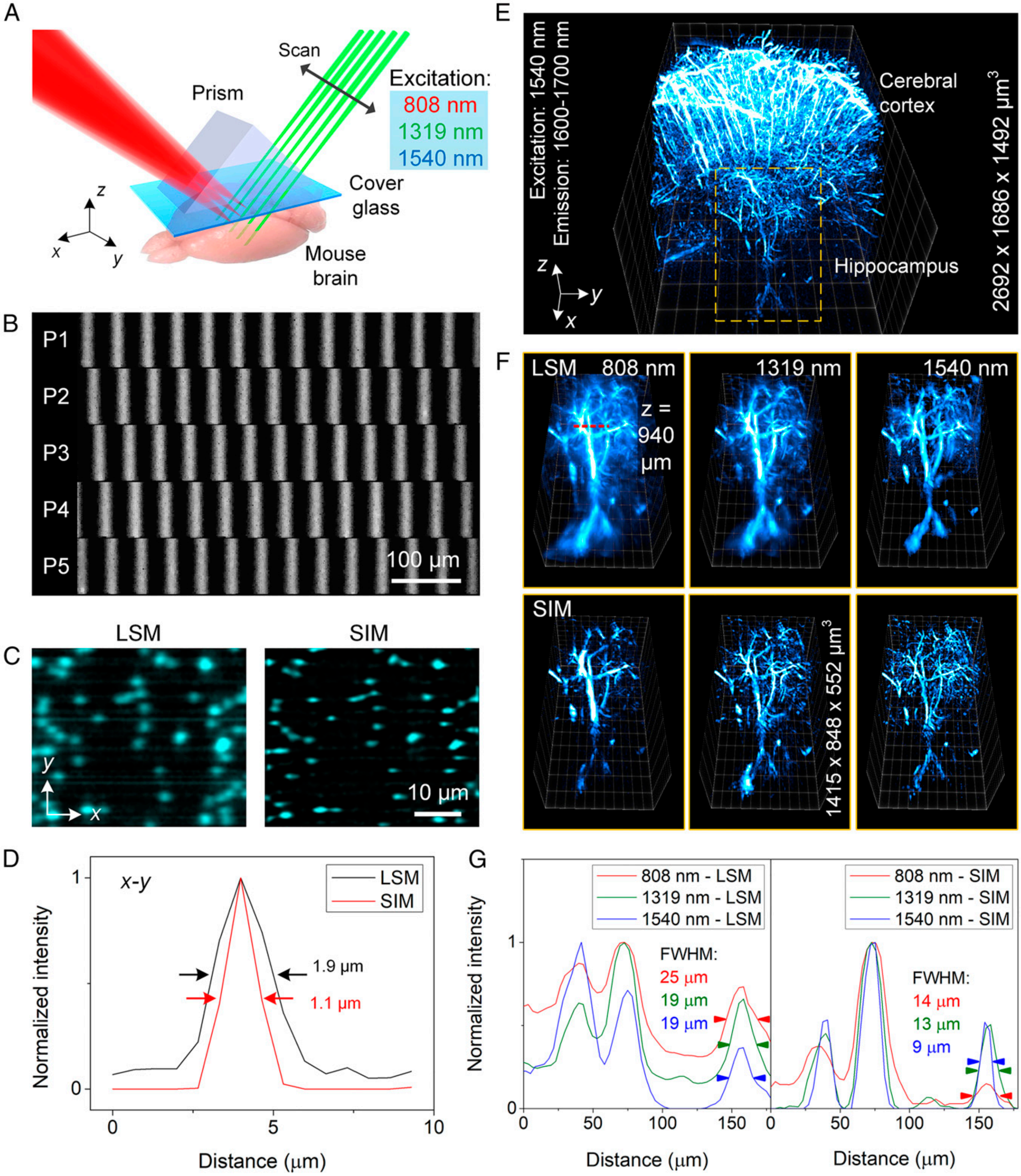

Fig. 1. Light-sheet microscopy with structured illumination in the near-infrared II window. (*A*) A simplified schematic of the oblique NIR-II SIM. (*B*) Structured illumination with five phases (P1 to P5) of NIR-II SIM. Light beam was formed by a 5× illumination objective with effective NA = 0.045 and imaged in water containing uniformly suspended PEGylated PbS/CdS CSQD. The fluorescence was collected in a 1,500- to 1,700-nm window excited by 1,319-nm illumination. (*C* and *D*) Comparation of LSM and SIM by imaging 300-nm-diameter p-FE nanoparticles at 658-nm excitation and a 1,100- to 1,700-nm collection window. p-FE nanoparticles were deposited on a coverslip. A 10× illumination objective and a 20× detection objective were used. (*E*) Volumetric 1,600- to 1,700-nm fluorescence imaging of PEGylated PbS/CdS CSQD-labeled vasculatures in glycerol-treated mouse brain optically sectioned by 1,540-nm structured illumination. A 4× illumination objective and a 5× detection objective were used. The scanning step was 4 μm along the *x* direction. (*F*) The 3D rendering of mouse hippocampus region at ~1-mm depth beneath the cerebral cortex surface and marked in *E* under different excitations (808, 1,319, and 1,540 nm). The 1,500- to 1,700-nm fluorescence was collected under 808- and 1,319-nm excitations and 1,600- to 1,700-nm fluorescence was collected for 1,540-nm illumination. The exposure times of the single-phase image were 150, 200, and 500 ms for 808-, 1,319-, and 1,540-nm excitations, respectively. (*G*) Normalized fluorescence intensity profiles along the red-dashed line in *F* for LSM and SIM, respectively. The raw intensity values were normalized by the maximum intensity along the red-dashed line.

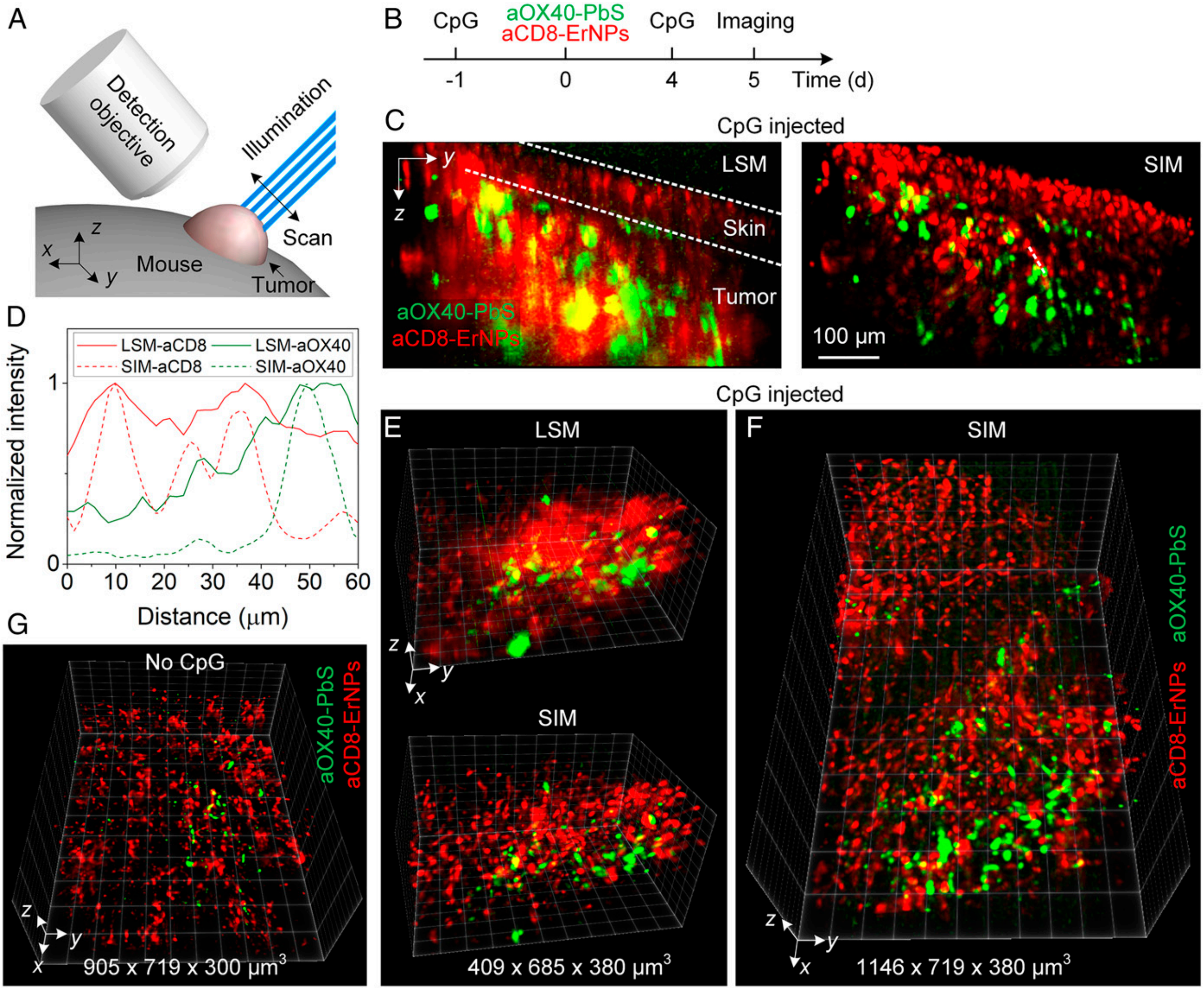

Fig. 2. Through-skin noninvasive in vivo NIR-II SIM imaging of CD8$^+$ T cells and OX40$^+$ cells in a CT26 tumor on a mouse. (*A*) Schematic of in vivo oblique NIR-II SIM with structured illumination and detection each at 45° to the normal of the tumor surface. (*B*) Treatment and imaging schedule. Two CT26 tumors were inoculated on the two hindlimbs of a BALB/c mouse. When the tumor size reached ∼4 mm (typically 3 to 4 d after inoculation), 50 μg CpG was injected into one of the two tumors. Two antibody conjugates aOX40-PbS and aCD8-ErNPs were intravenously injected through the mouse tail vain. (*C*) The maximum-intensity *x* projection recorded by LSM (*Left*) or SIM (*Right*) for a 300-μm-thick volume along *x* illustrating a cross-section of the CpG-treated CT26 tumor with aOX40-PbS (green) and aCD8-ErNPs (red). (*D*) Normalized two-channel fluorescence intensity profiles along the white-dashed line in *C* for LSM and SIM, respectively. (*E* and *F*) Noninvasive in vivo 3D LSM and SIM images of aOX40-PbS and aCD8-ErNPs in the same regions of a CpG-treated CT26 tumor. (*G*) NIR-II SIM of aOX40-PbS and aCD8-ErNPs in the distal nontreated tumor without CpG injection. (*E*–*G*) A 5× illumination objective and a 10× detection objective were used. The scanning step was 3 μm along the *x* direction. The exposure time of the single-phase image was 100 ms.

same NIR-IIb window (ErNPs, 1,500 to 1,700 nm; PbS/CdS CSQD, 1,600 to 1,700 nm), and two-plex molecular imaging of CD8 and OX40 was done by differentiating the different lifetimes of aCD8-ErNP (emission lifetime ∼10 ms) and aOX40-PbS (emission lifetime ∼40 μs) (31). As shown in the cross-section and 3D rotation results (Fig. 2 *C*–*F* and Movie S1), in vivo NIR-II SIM reached a vertical penetration depth of ∼350 μm into the tumor through an ∼80-μm-thick layer of highly scattering skin, revealing higher-resolution structural details than NIR-II LSM with the light sheet formed by a cylindrical lens (17). The SNR improved by approximately fourfold as structured illumination was introduced (Fig. 2*D*).

NIR-II SIM 3D imaging showed that CD8$^+$ T cells in the CpG-treated tumor expressed no OX40, evident by the lack of overlapping of CD8 and OX40 signals on the cells in both the CpG-treated and nontreated tumors (Fig. 2 *E*–*G*). This was consistent with previous ex vivo flow cytometry analysis showing absence of OX40 on CD8$^+$ T cells in the tumor microenvironment (52, 62, 63). On the other hand, regular NIR-II LSM molecular imaging (using a light sheet formed by a cylindrical lens) showed a degree of overlapping/coexistence of CD8 and OX40 on T cells (Fig. 2 *C* and *E*), attributed to an artifact caused by feature smearing that resulted in poorer spatial resolution and higher background. With NIR-II SIM imaging, we observed more abundant OX40$^+$ cells and CD8$^+$ T cells in the CpG-treated tumor (Fig. 2 *F* and *G*) than in the nontreated tumor at this timepoint by ∼1.7 times and ∼1.5 times, respectively. This was consistent with the ex vivo observation that CpG injection led to rapid CD8$^+$ T cell accumulation in the treated tumor site, which was essential to antitumor therapeutic effects (50, 52, 64).

Next, we imaged OX40- and CD4-expressed cells in the tumor microenvironment on a mouse 24 h after intratumoral injection of 50 μg CpG into one of the two CT26 tumors inoculated on the two hindlimbs. We first performed wide-field whole-body NIR-II fluorescence molecular imaging over time and observed higher aOX40-PbS and aCD4-ErNPs signals in the CpG-injected tumor than in the nontreated tumor (Fig. 3 *A* and *B*). The OX40 level in the CpG-injected tumor increased obviously with a tumor-to-normal-tissue (T/NT) ratio reaching a maximum of 22.6 ± 1.7 (compare to 13.5 ± 1.2 in nontreated tumor) 24 h postinjection (p.i.) of the probes. No such difference in OX40 levels was observed in the two tumors without any CpG injection (Fig. 3 *C* and *D* and *SI Appendix*, Fig. S7). A slightly higher T/NT ratio in the CD4 level labeled by aCD4-ErNPs in the CpG-treated tumor was also observed (treated tumor, 18.8 ± 1.6; nontreated tumors, 13.2 ± 1.7 at 24 h p.i.), suggesting CpG injection led to an increase in intratumoral CD4 T cells (50, 52). In contrast, the T/NT ratios measured with similarly injected, antibody-free PbS and ErNPs in both the CpG-treated and the nontreated tumor mouse were only ∼5 (at 24 h p.i.), much lower than the T/NT ratios measured in the treated tumor with injected aOX40-PbS and aCD4-ErNPs (*SI Appendix*, Fig. S8 and Fig. 3). These in vivo imaging data were consistent with ex vivo flow cytometry and in vivo PET imaging results of intratumoral CpG treatment up-regulating OX40 expression on CD4 T cells (52), leading to higher T/NT ratio of OX40 signals in the treated tumor. However, like PET imaging, whole-body wide-field NIR-II imaging lacked spatial resolution and was unable to reveal OX40 and CD4 expression at the cellular level inside the tumor.

We then performed two-plex NIR-II SIM in vivo molecular imaging to map out 3D spatial distribution of aOX40-PbS and aCD4-ErNPs in CpG-injected and nontreated tumors on the mouse (Fig. 3 *C* and *D*). Again, compared to LSM, NIR-II SIM afforded sharper images, higher cellular resolution, and higher SBR than regular NIR-II LSM (*SI Appendix*, Fig. S9). A 3D NIR-II SIM image inside a CT26 tumor recorded 3 h after intravenous injection of aOX40-PbS and aCD4-ErNPs (Fig. 4*A*) showed the structures of tumor vasculatures as the aOX40-PbS and aCD4-ErNPs probes were mainly in the blood circulation prior to extravasation into the tumor microenvironment.

At 24 h postinjection, NIR-II SIM imaging clearly revealed expression of OX40 and CD4 within the tumor labeled by the extravasated nanoprobes (Fig. 4 *B* and *C*), consistent with low-resolution whole-body imaging (Fig. 3 *C* and *D*). The OX40 signals obviously overlapped with CD4 signals on individual cells resolved in the tumor, suggesting abundant CD4$^+$ T cells with OX40 coexpression. This contrasted strongly with CD8$^+$ T cells

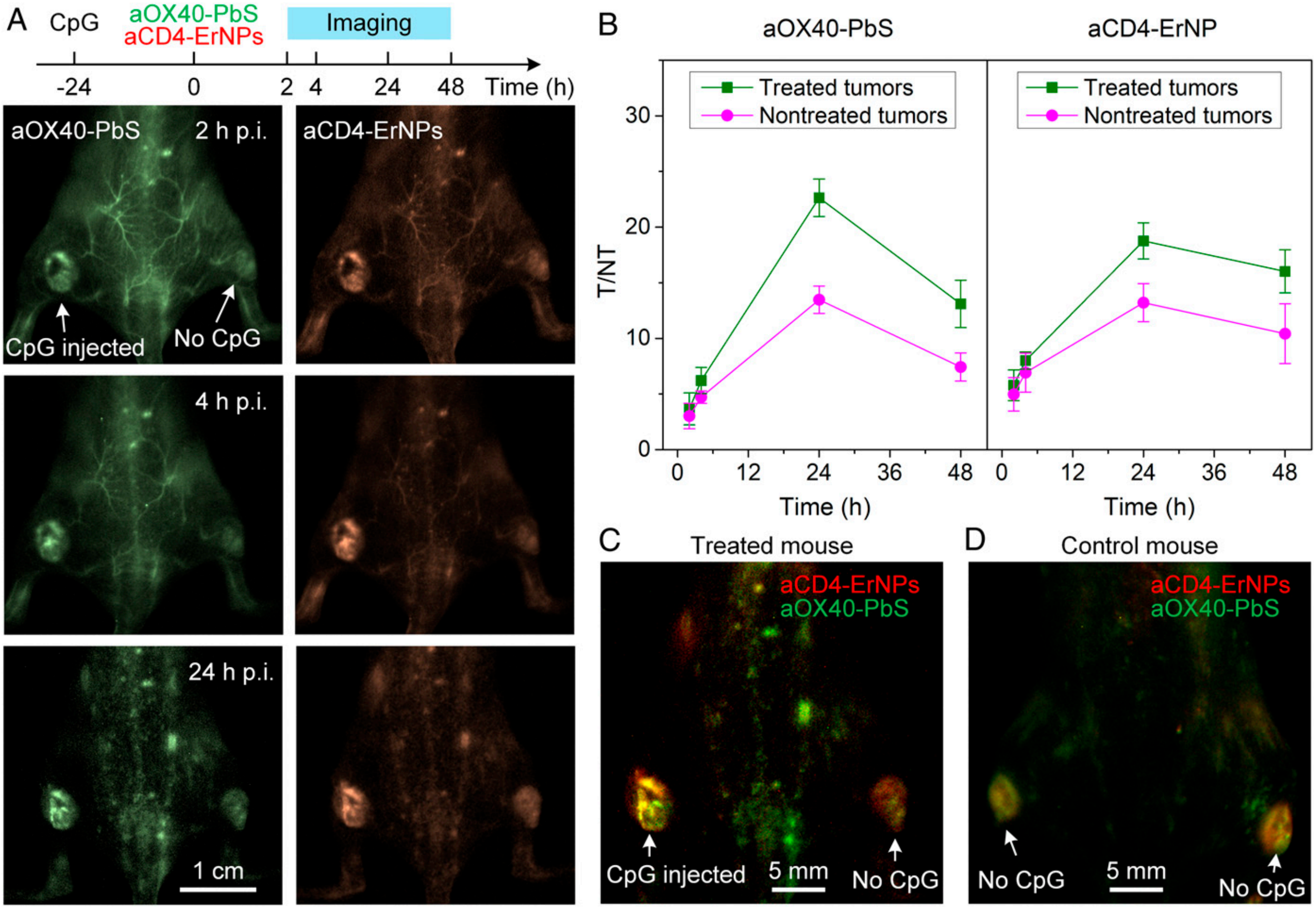

Fig. 3. Wide-field NIR-IIb molecular imaging of up-regulation of OX40 on CD4$^+$ T cells in a CpG-injected tumor. (*A*, *Top*) Treatment and imaging schedule. BALB/c mice were implanted subcutaneously with CT26 tumor cells on both the right and left hindlimbs. When the tumor size reached ∼4 mm (typically 3 to 4 d after inoculation), 50 μg CpG was injected into one tumor site 24 h before intravenous injection of aOX40-PbS and aCD4-ErNPs. (*A*, *Bottom*) Wide-field NIR-IIb fluorescence images of a mouse bearing two CT26 tumors with left tumor treated with CpG at various timepoints (2, 4, and 24 h p.i. as indicated) after injection of aOX40-PbS and aCD4-ErNPs. Similar results were obtained for $n = 3$ mice. (*B*) T/NT ratios of aOX40-PbS and aCD4-ErNPs from 2 to 48 h p.i. Data are shown as mean ± SD by analyzing $n = 3$ independent experiments. (*C* and *D*) Two-plex molecular imaging of mice bearing two CT26 tumors at 24 h post-intravenous injection of aCD4-ErNPs (red) and aOX40-PbS (green). (*C*) Image of a mouse with left tumor injected with CpG. (*D*) Image of a control mouse without CpG treatment.

https://doi.org/10.1073/pnas.2023888118

with barely any overlapping OX40 signals (Fig. 2). We observed a greater number of CD4$^+$ cells overexpressing OX40 in the microenvironment of the CpG-injected tumor than in the nontreated tumor (Fig. 4*B*), evident from the obviously more abundant yellow color-coded cells (due to overlapping of CD4 red-color coding and OX40 green-color coding; Fig. 4*B*, *Bottom*) in the former. Quantitative analysis showed ~91% of CD4$^+$ T cells expressing OX40 in the CpG-injected tumor vs. ~57% in the noninjected tumor (Fig. 4*E*). This result was consistent with intratumoral CpG injection inducing OX40 up-regulation on CD4$^+$ T cells by ex vivo flow cytometry analysis (52, 54, 57). Indeed, in a control experiment without any CpG injection, NIR-II SIM imaging showed similar, lower OX40 expression levels on CD4$^+$ cells in both the left and right tumors on a mouse (Fig. 4*C*).

Noninvasive NIR-II SIM In Vivo Imaging of CpG and Anti-OX40 Immunotherapy. NIR-II SIM is useful for noninvasive dynamic imaging and longitudinal monitoring at the cellular level over long periods of time. We performed 3D in vivo molecular imaging in the tumor microenvironment in response to CpG and anti-OX40 combined immunotherapy. Intratumoral injection of CpG locally up-regulated OX40 expression on CD4$^+$ T cells and simultaneous injection of agonistic anti-OX40 antibody could trigger a T cell specific immune response, effectively eliminating local and distal tumors in mice (57–59).

We injected 50 μg CpG and 8 μg anti-OX40 into one of the two CT26 tumors on the hindlimbs of a BALB/c mouse, 2 h later injected aCD4-ErNPs and aCD8-PbS intravenously, and performed wide-field NIR-II fluorescence molecular imaging over time (Fig. 5*A*). The T/NT ratios of CD4 and CD8 signals reached maxima ~24 h posttreatment, higher in the CpG/anti-OX40 injected tumor than in nontreated tumor (Fig. 5 *B* and *C*), with the difference in CD4 levels in the two tumors diminishing faster than CD8 levels (Fig. 5*C*). In a control experiment without CpG and anti-OX40 injection, no difference between the tumors was discerned (*SI Appendix*, Fig. S10). These observations revealed faster initial T cell responses in the tumor injected with CpG and anti-OX40, but over time similar T cell populations were also observed in the nontreated tumor, suggesting a systemic response elicited by local treatment (52).

Four days after CpG and anti-OX40 treatment, anti-OX40 labeled by an organic dye (65) (IR12, emission detected in the 1,000- to 1,200-nm range under excitation of 808 nm) was injected intravenously for molecular imaging of OX40 in the tumor microenvironment (Fig. 5*A*). Multiplexed longitudinal NIR-II SIM imaging of CD8 (PbS label), CD4 (ErNPs label), and OX40 (IR12 label) over 120 h was performed to monitor immune responses at the cellular level in tumor microenvironments (Fig. 5 *D* and *E*). The CpG and anti-OX40 injected tumor showed much higher aOX40-IR12 signal than the nontreated tumor 24 h postinjection of aOX40-IR12 (Fig. 5 *B* and *C*) and NIR-II SIM results revealed more OX40$^+$ CD4$^+$ T cells in the treated tumor than in the distal tumor (Fig. 5*E* and *SI Appendix*, Fig. S11), suggesting intratumor injection of CpG only locally up-regulated OX40 expression that persisted longer than 5 d. Meanwhile, we observed a greater number of CD8$^+$ and CD4$^+$ T cells in the microenvironment of CpG and anti-OX40 injected tumor than in the nontreated tumor by ~2-fold and ~1.3-fold, respectively, at 24 h postinjection of aCD4-ErNPs and aCD8-PbS. The amount of CD4$^+$ and CD8$^+$ T cells in the nontreated tumor gradually increased (Fig. 5*E* and *SI Appendix*, Fig. S11) over which we observed high-motility CD8$^+$ T cells in the nontreated tumor microenvironment (Fig. 5*D* and Movie S2). At 72 h p.i., the CD4$^+$ and CD8$^+$ cell counts per volume in the treated and nontreated tumor reached similar levels (*SI Appendix*, Fig. S11).

After intratumoral injection of CpG and anti-OX40, we observed tumor suppression and complete regression of the treated tumor in 5 to 7 d, followed by suppression and disappearance of the distal nontreated tumor 2 to 3 d later (52), consistent with delayed CD8$^+$ T cell responses in the nontreated tumor as observed by NIR-II SIM (Fig. 5). Taken together, multiplexed NIR-II SIM molecular imaging elucidated the immune responses in the tumor microenvironment at the cellular level, offering a noninvasive approach to investigating immunotherapy in mouse models.

Discussion

Light-sheet microscopy has attracted tremendous attention for biological and medical research due to its 3D volumetric imaging capability, low phototoxicity, low background, and fast sectioning speed (3). Decades of efforts have been taken to enhance resolution, volumetric imaging rate, and tissue penetration depth. Scanning structured illumination (2, 11–14, 23) and single-molecule localization (66, 67) have enabled LSM with subdiffraction limited resolution. As motorized stages are replaced by galvo mirrors for 3D scanning, over 300 vol/s has been reported (10, 16, 68, 69). The penetration depth can be increased using two-photon excitation, self-reconstructing Bessel (19, 20), or Airy beams (21). Our recently reported NIR-II LSM extended excitation and emission of up to 1,320 and 1,700 nm, respectively, suppressing light scattering for both excitation and emission. NIR-II LSM affords optical sectioning and volumetric imaging reaching a penetration depth up to ~750 μm through the intact scalp and skull of mice without craniotomy (17). However, the resolution of NIR-II LSM using a typical planar light sheet by a cylindrical lens is approximately two to three times lower than that of visible LSM due to diffraction limitation to the long wavelengths of light detected. Although NIR-II LSM allowed deeper penetration than visible LSM, it still experienced light scattering effects causing feature smearing and undesired background.

This work developed structured-illumination NIR-II LSM for in vivo and ex vivo optical sectioning of highly scattering tissues. Structured illumination is a widely pursued approach to overcoming the diffraction limit for 3D microscopy (43, 70). The seminal work by Gustafsson (43) showed that when a structured illumination (containing a frequency $\boldsymbol{k}$ in reciprocal space) was applied, the unresolvable high-frequency sample feature (with frequency of $\boldsymbol{k}'$) was embedded into Moiré fringes with a lower frequency ($\boldsymbol{k}' - \boldsymbol{k}$) (larger spacing in real space), which could be resolved by microscopy when $\boldsymbol{k}' - \boldsymbol{k} < k_0$ was satisfied. Imaging with phase shifting using the finest possible modulated-illumination, deconvolution of the high-frequency features can lead to higher-resolution features up to $k' \sim 2k_0$, corresponding to approximately twofold spatial resolution improvement (26, 66). Further, as the fluorescence from the focal plane modulated by structured illumination could be separated from the unmodulated out focus signal caused by scattering, SIM enables filtering out scattered light from ballistic light to afford lower background and higher SBR imaging.

In our case, even though extending one-photon excitation and emission up to >1,500 nm and 1,600 to 1,700 nm, respectively, enabled deep tissue in vivo imaging, residual light scattering still caused feature smearing, lowered spatial resolution, and led to artifactual overlapping of molecule signals on T cells (Fig. 2 and *SI Appendix*, Fig. S9). With NIR-II SIM, background and feature-smearing problems were suppressed, and the ~2× increased spatial resolution allowed more faithful molecular imaging at the cellular level in vivo.

NIR-II SIM affords a spatial resolution close to two- or multiphoton microscopy (~0.96 × 0.96 × 4.6 μm using an objective with NA = 1.05) (71, 72) without the need of an invasive imaging window installation. Higher resolution could be realized by using a pair of excitation and detection objectives with larger NA and long working distance. Nonlinear fluorescence emission could be introduced to achieve theoretically unlimited resolution (26). NIR-II SIM can also be further improved by using nonlinear

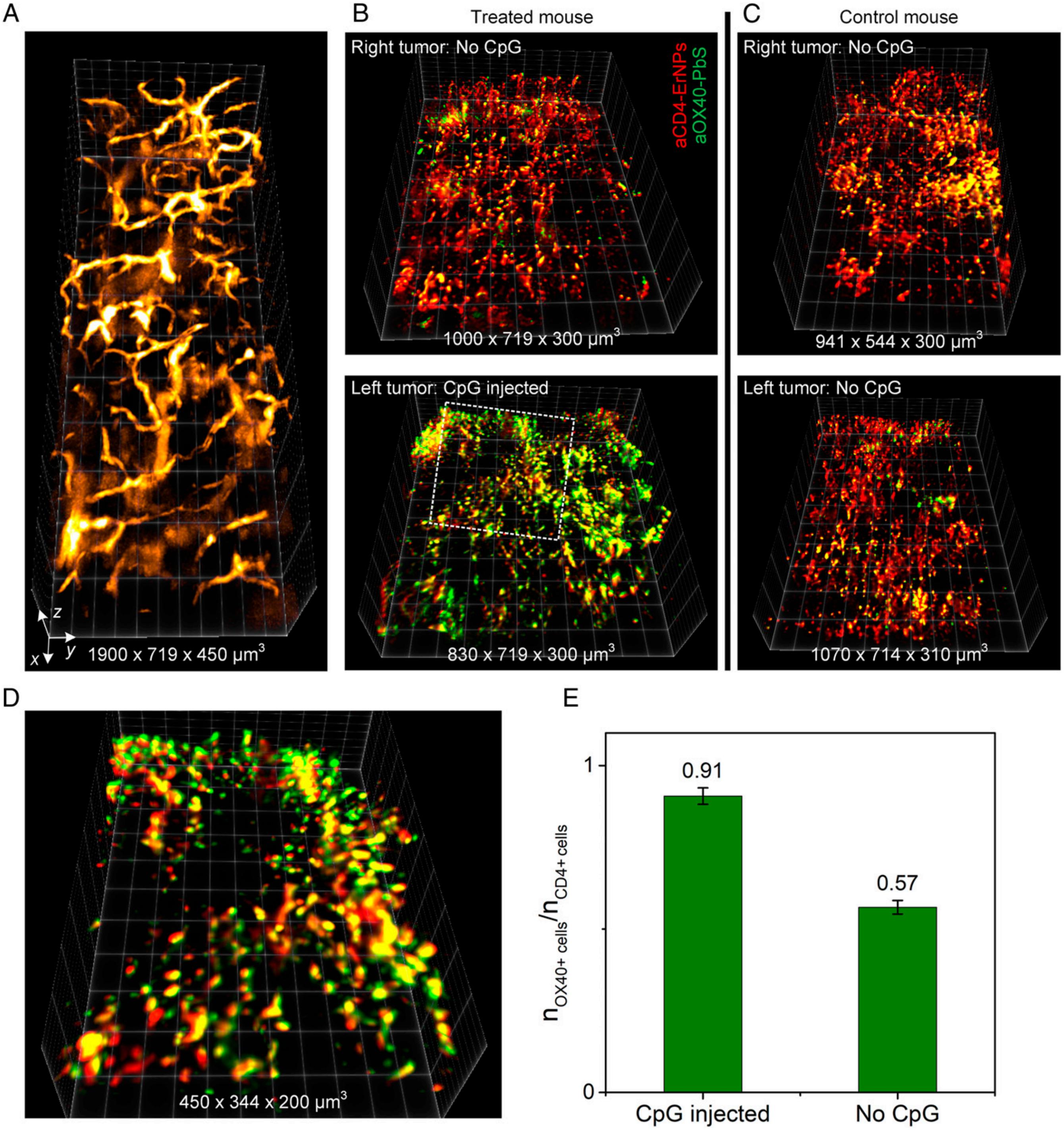

Fig. 4. Through-skin noninvasive in vivo two-plex molecular imaging of OX40 and CD4 in tumor microenvironment by NIR-IIb SIM. (*A*) A 3D reconstructed image of blood vessels in a CT26 tumor obtained 3 h after intravenous injection of aCD4-ErNPs and aOX40-PbS by NIR-II SIM. Imaging was done in NIR-IIb SIM mode by detecting the 1,600- to 1,700-nm fluorescence from aOX40-PbS circulating in blood vessels under a 1,540-nm structured illumination. (*B*) A 3D volumetric NIR-II SIM of aCD4-ErNPs (red) and aOX40-PbS (green) in the nontreated (*Top*) and CpG-injected (*Bottom*) tumors 24 h after intravenous injection of aCD4-ErNPs and aOX40-PbS (as shown in Fig. 3*C*) into a BALB/c mouse implanted subcutaneously with CT26 tumor cells on both the right and left hindlimbs. CpG treatment was performed on the left tumor 24 h before injection of labels when the tumor size reached ∼4 mm. (*C*) The same as in *B* for a mouse with left and right tumors without any CpG treatment. For *B* and *C* the exposure time of a single-phase image was 100 ms and the scanning step was 3 μm along the *x* direction. A 5× illumination objective and a 10× detection objective were used. (*D*) A higher-resolution NIR-II SIM imaging of a CpG-treated tumor by using a 10× illumination objective and a 20× detection objective corresponding to the marked volume in *B*. (*E*) The ratio of cells expressing OX40 and CD4 in treated and nontreated tumors in *B* measured from the SIM images recorded at 24 h postintravenous injection of aCD4-ErNPs and aOX40-PbS. CpG treatment was performed on one tumor site 24 h before injection of labels. Data are shown as mean ± SD derived from analyzing $n = 3$ independent experiments.

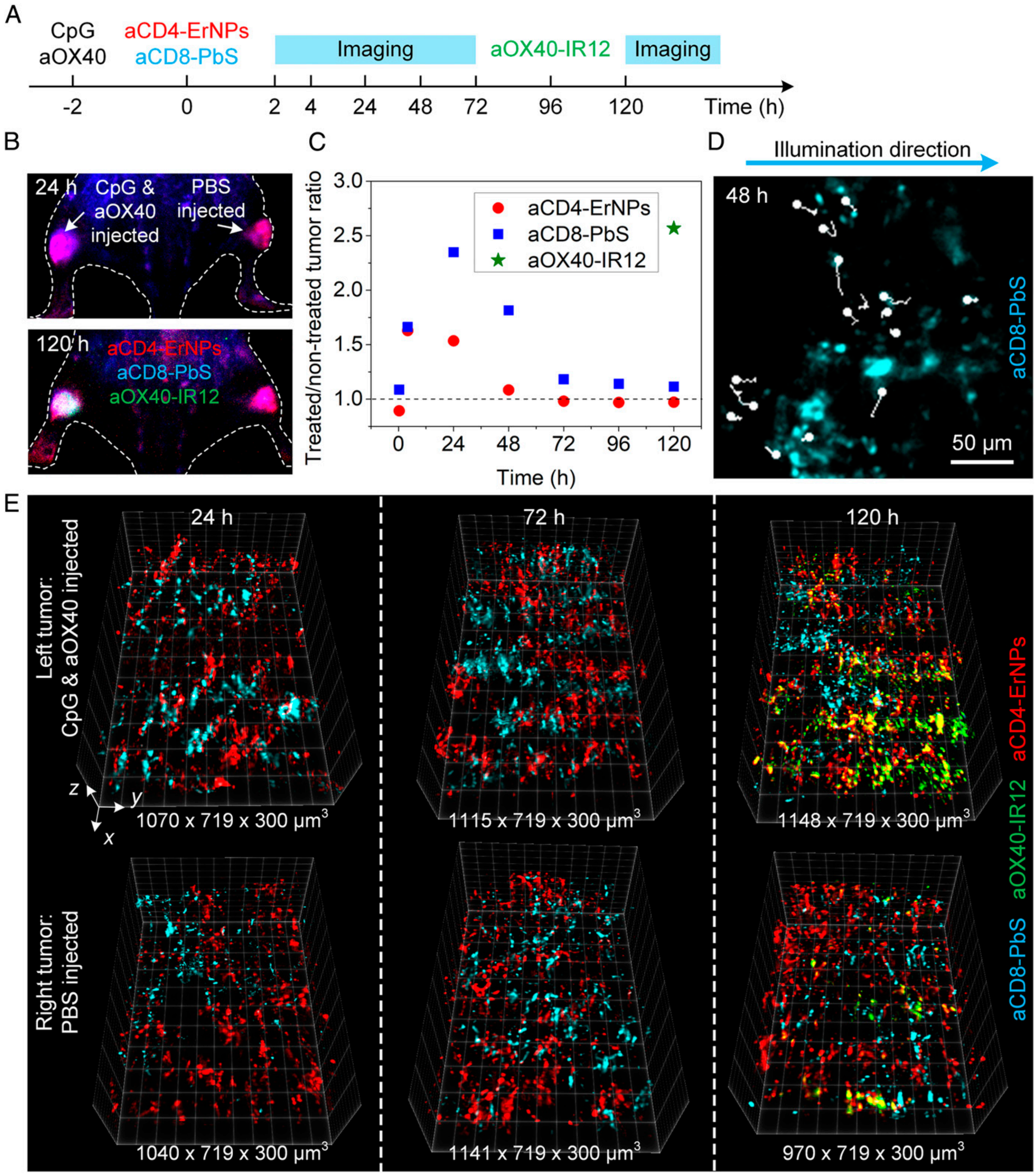

Fig. 5. Three-plex molecular imaging and longitudinal tracking of immune responses to combined CpG and OX40 antibody immunotherapy. (*A*) Treatment and imaging schedule. BALB/c mice were implanted subcutaneously with CT26 tumor cells on both the left and right hindlimbs. When the tumors reached ∼4 mm in size, 50 μg CpG and 8 μg anti-OX40 were injected into one tumor and phosphate-buffered saline (PBS) was injected into the other tumor 2 h before intravenous injection of aCD8-PbS and aCD4-ErNPs for imaging CD8 and CD4, respectively. Ninety-six hours later, aOX40-IR12 was injected intravenously for imaging OX40. (*B*) Wide-field NIR-IIb fluorescence images of a mouse bearing two CT26 tumors with left tumor treated by CpG and anti-OX40 at 24 h (*Top*) and 120 h (*Bottom*) after injection of aCD4-ErNPs (red) and aCD8-PbS (blue). aOX40-IR12 was colored green in *Bottom* image. (*C*) Fluorescence signal ratios of aCD4-ErNPs, aCD8-PbS, and aOX40-IR12 in the treated tumor to the nontreated tumor at different timepoints. (*D*) A snapshot of time-course NIR-II SIM imaging with trajectories of CD8$^+$ T cells within 45 min in the nontreated tumor 48 h after injection of aCD4-ErNPs and aCD8-PbS (cyan). Tracks are marked by white curves. (*E*) Noninvasive longitudinal 3D NIR-II SIM of aCD4-ErNPs, aCD8-PbS, or aOX40-IR12 in CpG and anti-OX40 treated (*Top*) and nontreated (*Bottom*) tumors 24, 72, and 120 h after intravenous injection of aCD4-ErNPs and aCD8-PbS. (*D* and *E*) A 5× illumination objective and a 10× detection objective were used. The exposure time of the single-phase image was 100 to 150 ms and the scanning step was 4 μm along the *x* direction.

excitation with Bessel beam (23) or optical-lattice illumination (2) to fully suppress background and increase resolution. Faster 3D imaging speed can be realized by using the single-objective configuration and galvo mirrors-based volumetric scanning methods (10, 16, 68).

NIR-II SIM is a noninvasive intravital imaging method for resolving cellular structures in vivo. Previous intravital imaging modalities included confocal microscopy (73), two-photon microscopy (74), or multiphoton microscopy (75), all of which have been used to investigate responses of the immune system to immunotherapy. For normal brain tissue, the penetration depth of two- or three-photon microscopy can be as deep as >1 mm (72, 76). However, only 300- to 500-µm depth for brain tumor (74, 77) and 200-µm depth for prostate tumor (78) have been claimed by using two- or multiphoton microscopy. The fluorescence signal containing high-frequency information deteriorates quickly after penetrating ∼150-µm tumor tissue due to its high scattering property (77, 78). Up to now, these tools have required installing transparent imaging windows on mice through invasive processes to circumvent high scattering caused by skin. NIR-II SIM is noninvasive by directly sectioning through the skin into tumor tissue, causing the least stress and perturbation to mice and achieving ∼350-µm penetration depth in the *z* direction or ∼500 µm along the illumination direction. Noninvasive or minimally invasive imaging can avoid undesired immune responses interfering with responses to immunotherapy (45, 46).

There is significant room for deploying NIR-II multiplexed molecular imaging for biology and medicine (17, 27–42). This work demonstrated three-plex in vivo molecular imaging by NIR-II SIM to investigate immune cells in response to immunotherapy with high spatial resolution. The longitudinal imaging ability of NIR-II SIM facilitated dynamic monitoring of CD4 and CD8 and OX-40 levels in response to treatment. Developing additional types of highly bright fluorescent or luminescent probes emitting in the NIR-II 1,000- to 1,700-nm range could allow imaging of a large set of molecular markers on cancer cells, T cells, B cells, and other cell types important to the innate and adaptive immune system. Exploiting time–life imaging in NIR-II for further multiplexing is also exciting. Developing genetically engineered NIR-II probes would also be exciting and important.

Materials and Methods

The materials and methods used in this study are described in detail in *SI Appendix, Materials and Methods*. Information includes descriptions of NIR-II fluorescent probes used in this study, NIR-II SIM setup and data analysis, resolution consideration in NIR-II SIM, mouse handling methods, wide-field NIR-II fluorescence imaging, in vivo NIR-II SIM of tumors, and temporal and spatial alignment for multichannel imaging by SIM.

Data Availability. All study data are included in this article and/or *SI Appendix*.

ACKNOWLEDGMENTS. This study was supported by the NIH Grant DP1-NS-105737.

1. M. J. Pittet, R. Weissleder, Intravital imaging. *Cell* **147**, 983–991 (2011).
2. T. L. Liu *et al*., Observing the cell in its native state: Imaging subcellular dynamics in multicellular organisms. *Science* **360**, eaaq1392 (2018).
3. J. Huisken, J. Swoger, F. Del Bene, J. Wittbrodt, E. H. Stelzer, Optical sectioning deep inside live embryos by selective plane illumination microscopy. *Science* **305**, 1007–1009 (2004).
4. H. U. Dodt *et al*., Ultramicroscopy: Three-dimensional visualization of neuronal networks in the whole mouse brain. *Nat. Methods* **4**, 331–336 (2007).
5. T. V. Truong, W. Supatto, D. S. Koos, J. M. Choi, S. E. Fraser, Deep and fast live imaging with two-photon scanned light-sheet microscopy. *Nat. Methods* **8**, 757–760 (2011).
6. A. Escobet-Montalbán *et al*., Three-photon light-sheet fluorescence microscopy. *Opt. Lett.* **43**, 5484–5487 (2018).
7. K. Chung *et al*., Structural and molecular interrogation of intact biological systems. *Nature* **497**, 332–337 (2013).
8. R. Tomer, L. Ye, B. Hsueh, K. Deisseroth, Advanced CLARITY for rapid and high-resolution imaging of intact tissues. *Nat. Protoc.* **9**, 1682–1697 (2014).
9. M. B. Bouchard *et al*., Swept confocally-aligned planar excitation (SCAPE) microscopy for high speed volumetric imaging of behaving organisms. *Nat. Photonics* **9**, 113–119 (2015).
10. R. Cai *et al*., Panoptic imaging of transparent mice reveals whole-body neuronal projections and skull-meninges connections. *Nat. Neurosci.* **22**, 317–327 (2019).
11. R. Gao *et al*., Cortical column and whole-brain imaging with molecular contrast and nanoscale resolution. *Science* **363**, eaau8302 (2019).
12. L. Gao *et al*., Noninvasive imaging beyond the diffraction limit of 3D dynamics in thickly fluorescent specimens. *Cell* **151**, 1370–1385 (2012).
13. L. Gao, L. Shao, B.-C. Chen, E. Betzig, 3D live fluorescence imaging of cellular dynamics using Bessel beam plane illumination microscopy. *Nat. Protoc.* **9**, 1083–1101 (2014).
14. B.-C. Chen *et al*., Lattice light-sheet microscopy: Imaging molecules to embryos at high spatiotemporal resolution. *Science* **346**, 1257998 (2014).
15. T. F. Holekamp, D. Turaga, T. E. Holy, Fast three-dimensional fluorescence imaging of activity in neural populations by objective-coupled planar illumination microscopy. *Neuron* **57**, 661–672 (2008).
16. V. Voleti *et al*., Real-time volumetric microscopy of in vivo dynamics and large-scale samples with SCAPE 2.0. *Nat. Methods* **16**, 1054–1062 (2019).
17. F. Wang *et al*., Light-sheet microscopy in the near-infrared II window. *Nat. Methods* **16**, 545–552 (2019).
18. H. Yu *et al*., *Biophotonics Congress: Biomedical Optics Congress (Microscopy/Translational/Brain/OTS) BF3C.3* (Optical Society of America, 2018).
19. F. O. Fahrbach, P. Simon, A. Rohrbach, Microscopy with self-reconstructing beams. *Nat. Photonics* **4**, 780–785 (2010).
20. O. E. Olarte *et al*., Image formation by linear and nonlinear digital scanned light-sheet fluorescence microscopy with Gaussian and Bessel beam profiles. *Biomed. Opt. Express* **3**, 1492–1505 (2012).
21. J. Nylk *et al*., Light-sheet microscopy with attenuation-compensated propagation-invariant beams. *Sci. Adv.* **4**, eaar4817 (2018).
22. P. J. Keller *et al*., Fast, high-contrast imaging of animal development with scanned light sheet-based structured-illumination microscopy. *Nat. Methods* **7**, 637–642 (2010).
23. T. A. Planchon *et al*., Rapid three-dimensional isotropic imaging of living cells using Bessel beam plane illumination. *Nat. Methods* **8**, 417–423 (2011).
24. M. Zhao *et al*., Cellular imaging of deep organ using two-photon Bessel light-sheet nonlinear structured illumination microscopy. *Biomed. Opt. Express* **5**, 1296–1308 (2014).
25. D. Xu, W. Zhou, L. Peng, Three-dimensional live multi-label light-sheet imaging with synchronous excitation-multiplexed structured illumination. *Opt. Express* **25**, 31159–31173 (2017).
26. M. G. L. Gustafsson, Nonlinear structured-illumination microscopy: Wide-field fluorescence imaging with theoretically unlimited resolution. *Proc. Natl. Acad. Sci. U.S.A.* **102**, 13081–13086 (2005).
27. H. Wan *et al*., Developing a bright NIR-II fluorophore with fast renal excretion and its application in molecular imaging of immune checkpoint PD-L1. *Adv. Funct. Mater.* **28**, 1804956 (2018).
28. M. Zhang *et al*., Bright quantum dots emitting at ∼1,600 nm in the NIR-IIb window for deep tissue fluorescence imaging. *Proc. Natl. Acad. Sci. U.S.A.* **115**, 6590–6595 (2018).
29. H. Wan *et al*., A bright organic NIR-II nanofluorophore for three-dimensional imaging into biological tissues. *Nat. Commun.* **9**, 1171 (2018).
30. Y. Zhong *et al*., Boosting the down-shifting luminescence of rare-earth nanocrystals for biological imaging beyond 1500 nm. *Nat. Commun.* **8**, 737 (2017).
31. Y. Zhong *et al*., In vivo molecular imaging for immunotherapy using ultra-bright near-infrared-IIb rare-earth nanoparticles. *Nat. Biotechnol.* **37**, 1322–1331 (2019).
32. Z. Ma *et al*., Near-infrared IIb fluorescence imaging of vascular regeneration with dynamic tissue perfusion measurement and high spatial resolution. *Adv. Funct. Mater.* **28**, 1803417 (2018).
33. G. Hong *et al*., Through-skull fluorescence imaging of the brain in a new near-infrared window. *Nat. Photonics* **8**, 723–730 (2014).
34. H. Wan, H. Du, F. Wang, H. Dai, Molecular imaging in the second near-infrared window. *Adv. Funct. Mater.* **29**, 1900566 (2019).
35. O. T. Bruns *et al*., Next-generation in vivo optical imaging with short-wave infrared quantum dots. *Nat. Biomed. Eng.* **1**, 0056 (2017).
36. S. Diao *et al*., Fluorescence imaging in vivo at wavelengths beyond 1500 nm. *Angew. Chem. Int. Ed. Engl.* **54**, 14758–14762 (2015).
37. G. Hong *et al*., Ultrafast fluorescence imaging in vivo with conjugated polymer fluorophores in the second near-infrared window. *Nat. Commun.* **5**, 4206 (2014).
38. S. Diao *et al*., Biological imaging without autofluorescence in the second near-infrared region. *Nano Res.* **8**, 3027–3034 (2015).
39. A. L. Antaris et *al*., A small-molecule dye for NIR-II imaging. *Nat. Mater.* **15**, 235–242 (2016).
40. N. Won *et al*., Imaging depths of near-infrared quantum dots in first and second optical windows. *Mol. Imaging* **11**, 338–352 (2012).
41. X. D. Zhang *et al*., Traumatic brain injury imaging in the second near-infrared window with a molecular fluorophore. *Adv. Mater.* **28**, 6872–6879 (2016).
42. Z. Ma *et al*., Cross-link-functionalized nanoparticles for rapid excretion in nanotheranostic applications. *Angew. Chem. Int. Ed. Engl.* **59**, 20552–20560 (2020).
43. M. G. L. Gustafsson, Surpassing the lateral resolution limit by a factor of two using structured illumination microscopy. *J. Microsc.* **198**, 82–87 (2000).
44. H. M. J. Werner, G. B. Mills, P. T. Ram, Cancer systems biology: A peek into the future of patient care? *Nat. Rev. Clin. Oncol.* **11**, 167–176 (2014).
45. A. Maeda *et al*., In vivo optical imaging of tumor and microvascular response to ionizing radiation. *PLoS One* **7**, e42133 (2012).

46. A. Benbenishty *et al*., Prophylactic TLR9 stimulation reduces brain metastasis through microglia activation. *PLoS Biol.* **17**, e2006859 (2019).
47. G. Yang, F. Pan, C. N. Parkhurst, J. Grutzendler, W. B. Gan, Thinned-skull cranial window technique for long-term imaging of the cortex in live mice. *Nat. Protoc.* **5**, 201–208 (2010).
48. R. D. Dorand, D. S. Barkauskas, T. A. Evans, A. Petrosiute, A. Y. Huang, Comparison of intravital thinned skull and cranial window approaches to study CNS immunobiology in the mouse cortex. *Intravital* **3**, e29728 (2014).
49. K. Heckelsmiller *et al*., Peritumoral CpG DNA elicits a coordinated response of CD8 T cells and innate effectors to cure established tumors in a murine colon carcinoma model. *J. Immunol.* **169**, 3892–3899 (2002).
50. Y. L. Chen *et al*., ERK activation modulates cancer stemness and motility of a novel mouse oral squamous cell carcinoma cell line. *Cancers (Basel)* **12**, 61 (2019).
51. H. Wagner, The immunogenicity of CpG-antigen conjugates. *Adv. Drug Deliv. Rev.* **61**, 243–247 (2009).
52. I. Sagiv-Barfi *et al*., Eradication of spontaneous malignancy by local immunotherapy. *Sci. Transl. Med.* **10**, eaan4488 (2018).
53. A. D. Weinberg, A. T. Vella, M. Croft, OX-40: Life beyond the effector T cell stage. *Semin. Immunol.* **10**, 471–480 (1998).
54. B. D. Curti *et al*., OX40 is a potent immune-stimulating target in late-stage cancer patients. *Cancer Res.* **73**, 7189–7198 (2013).
55. C. E. Ruby, R. Montler, R. Zheng, S. Shu, A. D. Weinberg, IL-12 is required for anti-OX40-mediated CD4 T cell survival. *J. Immunol.* **180**, 2140–2148 (2008).
56. S. Aspeslagh *et al*., Rationale for anti-OX40 cancer immunotherapy. *Eur. J. Cancer* **52**, 50–66 (2016).
57. A. Marabelle *et al*., Depleting tumor-specific Tregs at a single site eradicates disseminated tumors. *J. Clin. Invest.* **123**, 2447–2463 (2013).
58. J. Qian *et al*., Active vaccination with Dickkopf-1 induces protective and therapeutic antitumor immunity in murine multiple myeloma. *Blood* **119**, 161–169 (2012).
59. K. S. Voo *et al*., Selective targeting of Toll-like receptors and OX40 inhibit regulatory T-cell function in follicular lymphoma. *Int. J. Cancer* **135**, 2834–2846 (2014).
60. A. M. Monjazeb *et al*., Blocking indolamine-2, 3-dioxygenase rebound immune suppression boosts antitumor effects of radio-immunotherapy in murine models and spontaneous canine malignancies. *Clin. Cancer Res.* **22**, 4328–4340 (2016).
61. R. Tavaré *et al*., An effective immuno-PET imaging method to monitor CD8-dependent responses to immunotherapy. *Cancer Res.* **76**, 73–82 (2016).
62. V. Tkachev *et al*., Combined OX40L and mTOR blockade controls effector T cell activation while preserving T_{reg} reconstitution after transplant. *Sci. Transl. Med.* **9**, eaan3085 (2017).
63. M. Pohl *et al*., T cell-activation in neuromyelitis optica lesions plays a role in their formation. *Acta Neuropathol. Commun.* **1**, 85 (2013).
64. D. B. Hoelzinger *et al*., Blockade of CCL1 inhibits T regulatory cell suppressive function enhancing tumor immunity without affecting T effector responses. *J. Immunol.* **184**, 6833–6842 (2010).
65. S. Zhu *et al*., 3D NIR-II molecular imaging distinguishes targeted organs with high-performance NIR-II bioconjugates. *Adv. Mater.* **30**, e1705799 (2018).
66. J. Kim *et al*., Oblique-plane single-molecule localization microscopy for tissues and small intact animals. *Nat. Methods* **16**, 853–857 (2019).
67. A.-K. Gustavsson, P. N. Petrov, M. Y. Lee, Y. Shechtman, W. E. Moerner, 3D single-molecule super-resolution microscopy with a tilted light sheet. *Nat. Commun.* **9**, 123 (2018).
68. C. Dunsby, Optically sectioned imaging by oblique plane microscopy. *Opt. Express* **16**, 20306–20316 (2008).
69. E. M. C. Hillman, V. Voleti, W. Li, H. Yu, Light-sheet microscopy in neuroscience. *Annu. Rev. Neurosci.* **42**, 295–313 (2019).
70. H. Rainer, G. C. Christoph, Laterally modulated excitation microscopy: improvement of resolution by using a diffraction grating. *Proc. SPIE* **3568**, 185–196 (1999).
71. T. Wang *et al*., Three-photon imaging of mouse brain structure and function through the intact skull. *Nat. Methods* **15**, 789–792 (2018).
72. N. G. Horton *et al*., *In vivo* three-photon microscopy of subcortical structures within an intact mouse brain. *Nat. Photonics* **7**, 205–209 (2013).
73. S. P. Arlauckas *et al*., In vivo imaging reveals a tumor-associated macrophage-mediated resistance pathway in anti-PD-1 therapy. *Sci. Transl. Med.* **9**, eaal3604 (2017).
74. Z. Chen, J. L. Ross, D. Hambardzumyan, Intravital 2-photon imaging reveals distinct morphology and infiltrative properties of glioblastoma-associated macrophages. *Proc. Natl. Acad. Sci. U.S.A.* **116**, 14254–14259 (2019).
75. S. Qi *et al*., Long-term intravital imaging of the multicolor-coded tumor microenvironment during combination immunotherapy. *eLife* **5**, e14756 (2016).
76. D. G. Ouzounov *et al*., In vivo three-photon imaging of activity of GCaMP6-labeled neurons deep in intact mouse brain. *Nat. Methods* **14**, 388–390 (2017).
77. C. Ricard, F. C. Debarbieux, Six-color intravital two-photon imaging of brain tumors and their dynamic microenvironment. *Front. Cell. Neurosci.* **8**, 57 (2014).
78. E. Dondossola *et al*., Intravital microscopy of osteolytic progression and therapy response of cancer lesions in the bone. *Sci. Transl. Med.* **10**, eaao5726 (2018).